NRL Report 8861

Elimination of Sensor Artifacts from Infrared Data

RICHARD STEINBERG

Advanced Concepts Branch
Optical Sciences Division

December 11, 1984

NAVAL RESEARCH LABORATORY
Washington, D.C.

SECUR. CLASSIFICATION OF THIS PAGE

REPORT DOCUMENTATION PAGE

1a. REPORT SECURITY CLASSIFICATION UNCLASSIFIED	1b. RESTRICTIVE MARKINGS
2a. SECURITY CLASSIFICATION AUTHORITY	3. DISTRIBUTION / AVAILABILITY OF REPORT Approved for public release; distribution unlimited.
2b. DECLASSIFICATION / DOWNGRADING SCHEDULE	
4. PERFORMING ORGANIZATION REPORT NUMBER(S) NRL Report 8861	5. MONITORING ORGANIZATION REPORT NUMBER(S)
6a. NAME OF PERFORMING ORGANIZATION Naval Research Laboratory 6b. OFFICE SYMBOL *(If applicable)*	7a. NAME OF MONITORING ORGANIZATION
6c. ADDRESS *(City, State, and ZIP Code)* Washington, DC 20375-5000	7b. ADDRESS *(City, State, and ZIP Code)*
8a. NAME OF FUNDING / SPONSORING ORGANIZATION 8b. OFFICE SYMBOL *(If applicable)*	9. PROCUREMENT INSTRUMENT IDENTIFICATION NUMBER
8c. ADDRESS *(City, State, and ZIP Code)*	10. SOURCE OF FUNDING NUMBERS PROGRAM ELEMENT NO. / PROJECT NO. / TASK NO. / WORK UNIT ACCESSION NO. EX380-280

11. TITLE *(Include Security Classification)*
Elimination of Sensor Artifacts from Infrared Data

12. PERSONAL AUTHOR(S)
Steinberg, R.

13a. TYPE OF REPORT	13b. TIME COVERED	14. DATE OF REPORT *(Year, Month, Day)*	15. PAGE COUNT
Interim	FROM _____ TO _____	1984 December 11	22

16. SUPPLEMENTARY NOTATION

17. COSATI CODES			18. SUBJECT TERMS *(Continue on reverse if necessary and identify by block number)*
FIELD	GROUP	SUB-GROUP	Infrared, BMAP, IRST, Data correction

19. ABSTRACT *(Continue on reverse if necessary and identify by block number)*

The objective of the Navy Background Measurements and Analysis Program (BMAP) is to satisfy the data requirements for design of surface- and air-based infrared (IR) search and track devices. The IR backgrounds data are acquired with a sensor that has high spatial resolution, high sensitivity, and simultaneous 4 to 5 μm/8 to 11 μm capability. Laboratory tests show that the 8 to 11 μm detector array has an undesired ground resistance that introduces weak electrical resistive coupling among the detector channels, giving rise to spatial defects in the long-wave data. Techniques are developed for inverting the focal plane resistive network, effectively decoupling the detector channels and eliminating the spatial artifacts, without smoothing the data or degrading noise performance.

20 DISTRIBUTION / AVAILABILITY OF ABSTRACT ☒ UNCLASSIFIED/UNLIMITED ☐ SAME AS RPT ☐ DTIC USERS	21. ABSTRACT SECURITY CLASSIFICATION
22a NAME OF RESPONSIBLE INDIVIDUAL Richard Steinberg	22b. TELEPHONE *(Include Area Code)* (202) 767-3045 22c. OFFICE SYMBOL Code 6520

DD FORM 1473, 84 MAR 83 APR edition may be used until exhausted.
All other editions are obsolete.

SECURITY CLASSIFICATION OF THIS PAGE

CONTENTS

ELIMINATION OF SENSOR ARTIFACTS FROM INFRARED DATA

BACKGROUND

The objective of the Navy Background Measurements and Analysis Program (BMAP) is to satisfy the data requirements for design of surface- and air-based infrared (IR) search and track devices [1,2]. The BMAP product is a test set of IR background images for use in off-line simulation of alternative signal processing techniques for false-alarm suppression. The sensor used to obtain the background data is an IR scanner constructed, owned, and operated by Raytheon Missile Systems Division, Bedford, MA. Table 1 summarizes the measurement system characteristics.

Table 1 — Technical Characteristics of the Raytheon Dual-band Scanner

Pixel size (mrad, square)	1/3
Elevation channels/waveband	16
Azimuth field-of-view	2.2°
Frame rate (frames/s)	1
Word depth (bits/sample)	12
Sample factor (samples/dwell)	3.44
NEI (w/cm^2, array average)	
3.9–4.8 μm	2.0×10^{-14}
7.6–11.3 μm	1.0×10^{-13}

The scanner's long-wave array consists of two columns of detectors, separated by a gold common deposited on the HgCdTe detector material. Ground connections are brought out from the gold common both from the top and from the bottom (Fig. 1). The long-wave array has 15 optically active elements, the first detector channel being inactive.

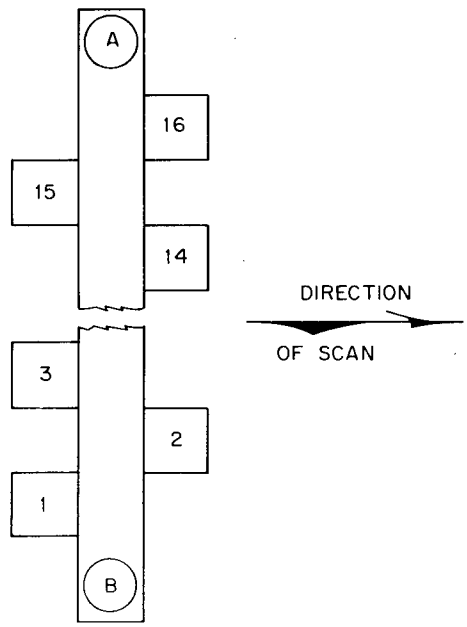

Fig. 1 — Geometry of long-wave photoconductive HgCdTe detector array. Each detector is square, 2 × 2 mil. The column of odd-numbered detectors is separated from the column of even-numbered detectors by a gold common 2 mils wide. Ground connections are made at points A and B on the gold common. Detector No. 1 is optically inactive.

Manuscript approved August 31, 1984.

The detector arrays are scanned in azimuth over approximately a 2.8° field of view. As each detector traverses its 2.8° azimuth sweep, the output voltage of its corresponding postamplifier is sampled 512 times. Thus each long-wave frame consists of a 15 × 512 matrix of numbers, where the small dimension corresponds to detector channel or elevation, and the long dimension corresponds to time or azimuth. Of the total 2.8° azimuth scan, about 0.6° (the first 100 samples) is filled by an internal calibration pulse. Thus the viewed scene external to the sensor is actually 2.2° in azimuth. We omit the calibration pulse in displaying the data. Censoring the first 112 samples, each long-wave frame then consists of a 15 × 400 matrix of numbers.

ARTIFACTS APPEAR IN BAR-TARGET SCANS

Laboratory bar-target measurements were performed in the interest of characterizing the transient response of the Raytheon dual-band scanner. Figure 2 shows a single frame of long-wave bar target data in three-dimensional (3-D) perspective format. The bar was oriented perpendicular to the direction of scan and had a 31.4°C contrast against its background. The data displayed in Fig. 2 have been processed by NRL as follows.

- Sample errors introduced by the digital data recorder were removed [1].
- The data for even-numbered channels were delayed seven samples relative to the data for odd-numbered channels to compensate the offset between even- and odd-channel detector columns (Fig. 1). The seven-sample offset follows from the sample rate, 3.44 samples per dwell, and the fact that the gold common has the same 2-mil width as the detector elements (Fig. 1). The distinction between the true two-dwell offset of 6.88 samples and the applied integral offset of 7 samples is not significant.
- Separate offset and gain parameters were calculated and applied to each detector channel to compensate detector responsivity nonuniformity.

Before inspecting the bar target measurements, it was expected that the preceding sequence of operations would constitute the major part of data reduction, the sole remaining step being a single additional gain and offset correction applied to the entire frame for radiometric calibration. This expectation was overly optimistic, however, as seen by inspection of Fig. 2. The horn-shaped spatial artifacts in the data are seen more clearly in Figs. 3 and 4, depicting channels 2 and 3 of the data frame shown in its entirety in Fig. 2. Data for all even-numbered channels are similar in appearance to those of Fig. 3, while data for all odd-numbered channels are similar in appearance to those of Fig. 4.

Raytheon engineers hypothesized that the long-wave data artifacts might be due to the resistance of the ground connections to the HgCdTe focal plane (Fig. 1), introducing a small amount of electrical resistive coupling among the detector channels. The present work confirms the resistive coupling hypothesis.

SUMMARY OF RESULTS

We show in our analysis that the resistive coupling artifact can be corrected by applying the following equation to the long-wave data:

$$E_n(t) = A_n^{-1}\left[I_n(t) + B_n \sum_{m=2}^{16} I_m(t)\right], \quad n = 2, 3, \ldots 16, \tag{1}$$

where n indexes the detector channel, t is time, and coefficients A_n and B_n, together, are 30 correction constants. The 15 waveforms $I_n(t)$, $n = 2, 3, \ldots 16$, entered as input to Eq. (1) are the digitized postamplifier outputs in need of correction (e.g., Figs. 3 and 4 show $I_2(t)$ and $I_3(t)$ for a given frame

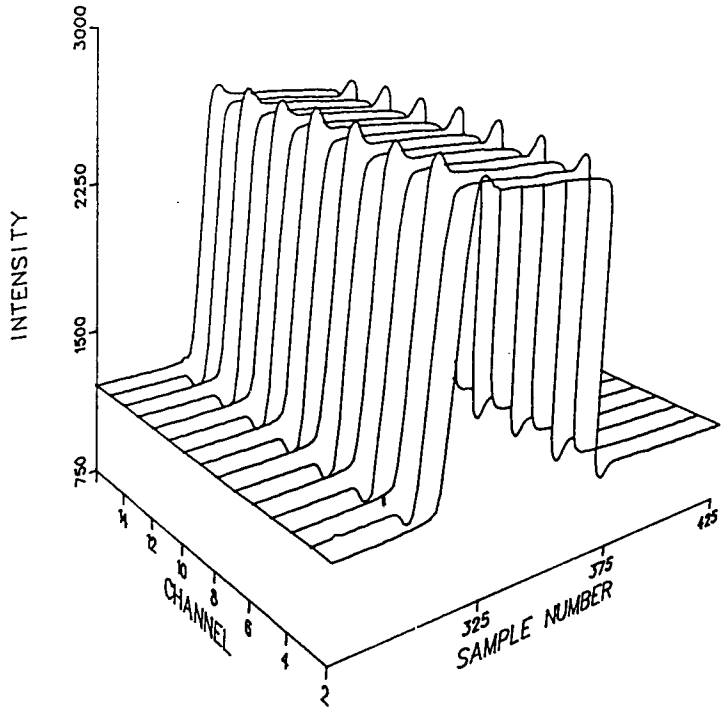

Fig. 2 — Frame of long-wave bar target data displaying spatial artifacts (horns) caused by resistive interchannel coupling. Bar target contrast temperature was 31.4°C. Sensor rms noise is about one unit on the y-axis scale, and hence is far below visibility on the scale of this drawing. Data have been processed by removing sample errors and by applying separate gain and offset constants to each channel for nonuniformity compensation.

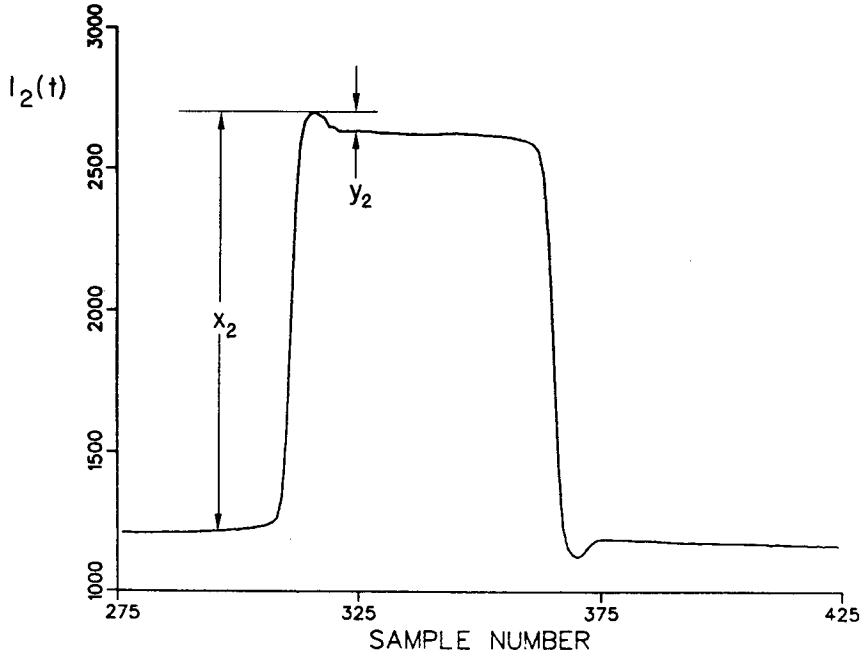

Fig. 3 — Postamplifier output waveform for LWIR channel 2, for data frame shown in its entirety as in Fig. 2. All even-numbered detector waveforms, 2, 4, ... 16, are similar in appearance.

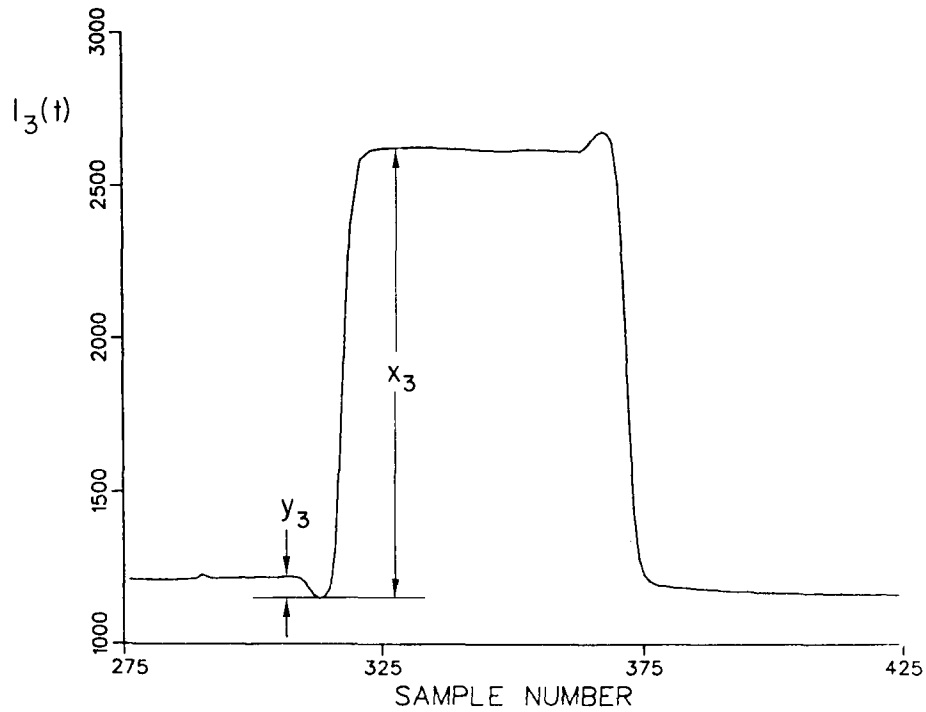

Fig. 4 — Postamplifier output waveform for LWIR channel 3, for data frame shown in its entirety as in Fig. 2. All odd-numbered detector waveforms, 3, 5, ... 15, are similar in appearance.

of data). The 15 waveforms $E_n(t)$, $n = 2, 3, \ldots 16$, are the corrected data. Equation (1) is "instantaneous," i.e., the corrected value $E_n(t_1)$ is generated from the 15 instantaneous samples $I_2(t_1)$, $I_3(t_1)$, $\ldots I_{16}(t_1)$, and does not depend on values of $I_n(t)$ for times $t \neq t_1$. The instantaneous, or "memoryless," property of Eq. (1) is characteristic of resistive coupling as opposed to, e.g., inductive or capacitive coupling. Since Eq. (1) is the same for all values of time, we generally unburden our notation by not showing explicit time dependence, i.e., by writing the waveform quantities $E_n(t)$ and $I_n(t)$ as E_n and I_n, respectively.

The 30 coefficients in Eq. (1), 15 values each of A_n and B_n, are determined from an analysis that requires as input the thirty parameters x_n, y_n obtained from one frame of bar target data. The parameters x_n and y_n are directly measurable from the original waveforms, as shown in Figs. 3 and 4. Waveform parameters x_n and y_n and the derived correction constants A_n^{-1} and B_n are given in Table 2.

The same bar-target frame in which the resistive coupling defect was originally manifest, Fig. 2, serves as the source of diagnostic data from which the correction constants are derived.

The effectiveness of the correction formula, Eq. (1), is illustrated by Figs. 5 to 7, depicting the corrected versions of Figs. 2 to 4. On average, the resistive coupling artifact is reduced tenfold (Table 3). Apparently, the correction is excellent when applied to data from which the correction constants are derived. An obvious question is whether the correction is data- or time-dependent, i.e., whether the correction constants derived from Fig. 2 will serve to correct data having different varieties of structure than Fig. 2, obtained some time subsequent to Fig. 2.

Table 2 — Waveform Parameters and Correction Constants for Long-Wave Detector Array. Waveform parameters are measured from a single frame of bar target data (Figs. 2, 3, and 4). Correction constants are used with Eq. (1) to perform data correction.

Detector Channel	Waveform Parameters		Correction Constants	
n	x_n	y_n	A_n^{-1}	$B_n(\times 10^{-2})$
2	1556	71	1.01947	0.68322
3	1535	74	1.01790	0.63862
4	1571	96	0.99304	0.92380
5	1562	87	0.99405	0.75082
6	1629	93	0.96181	0.89493
7	1613	110	0.95269	0.94931
8	1595	109	0.97060	1.04890
9	1547	111	0.99043	0.95794
10	1557	104	0.99591	1.00078
11	1557	104	0.98810	0.89753
12	1560	82	1.00925	0.78908
13	1510	100	1.01933	0.86301
14	1592	86	0.98741	0.82757
15	1492	80	1.04250	0.69041
16	1499	53	1.07017	0.51001

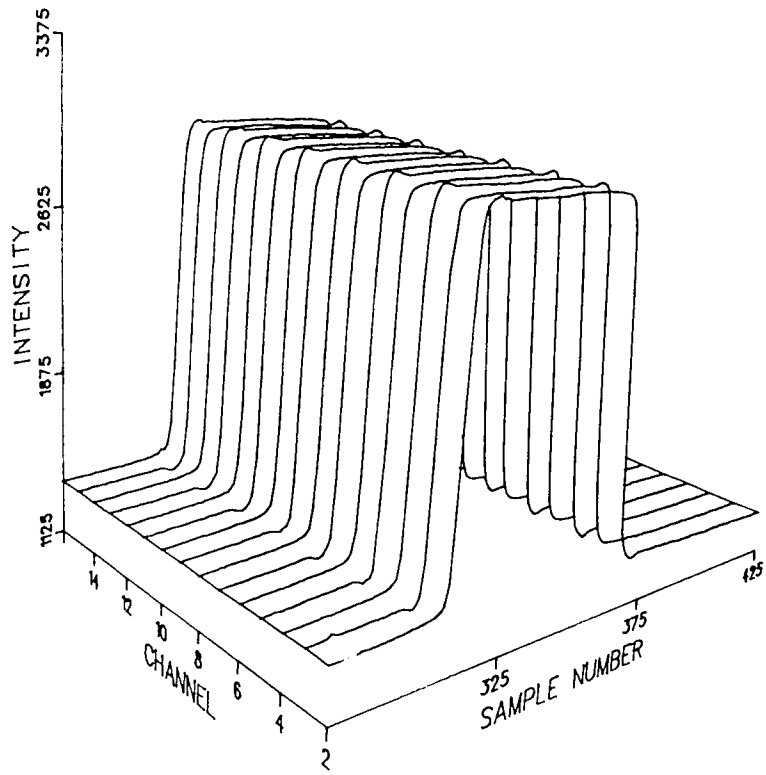

Fig. 5 — Entire frame of long-wave bar-target data, originally shown as Fig. 2, after resistive coupling correction

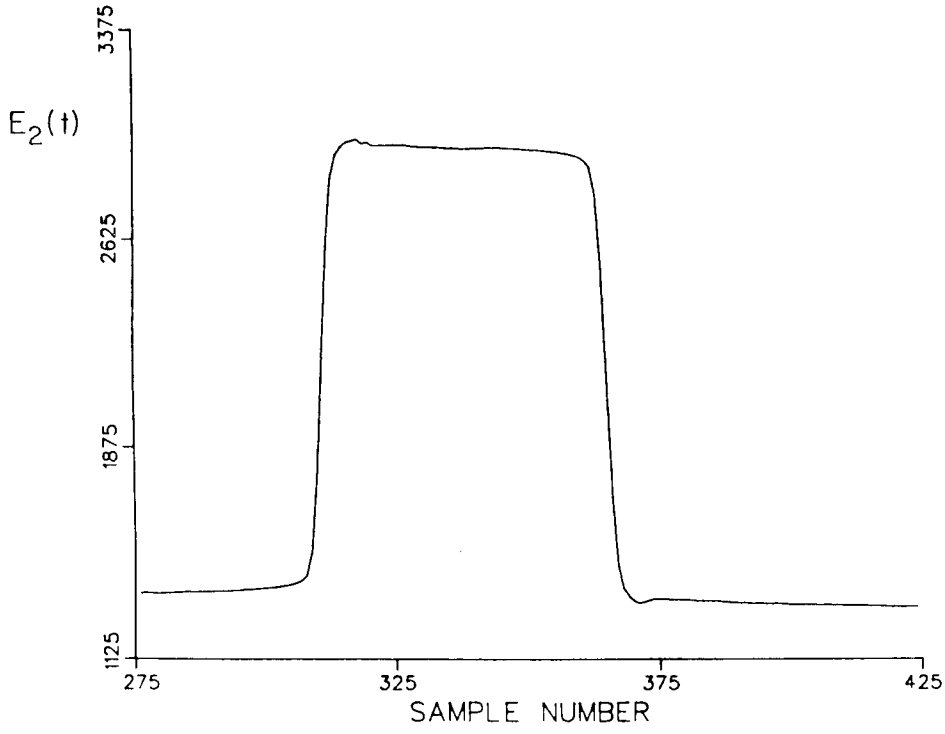

Fig. 6 — Channel 2 of corrected data, extracted from Fig. 5

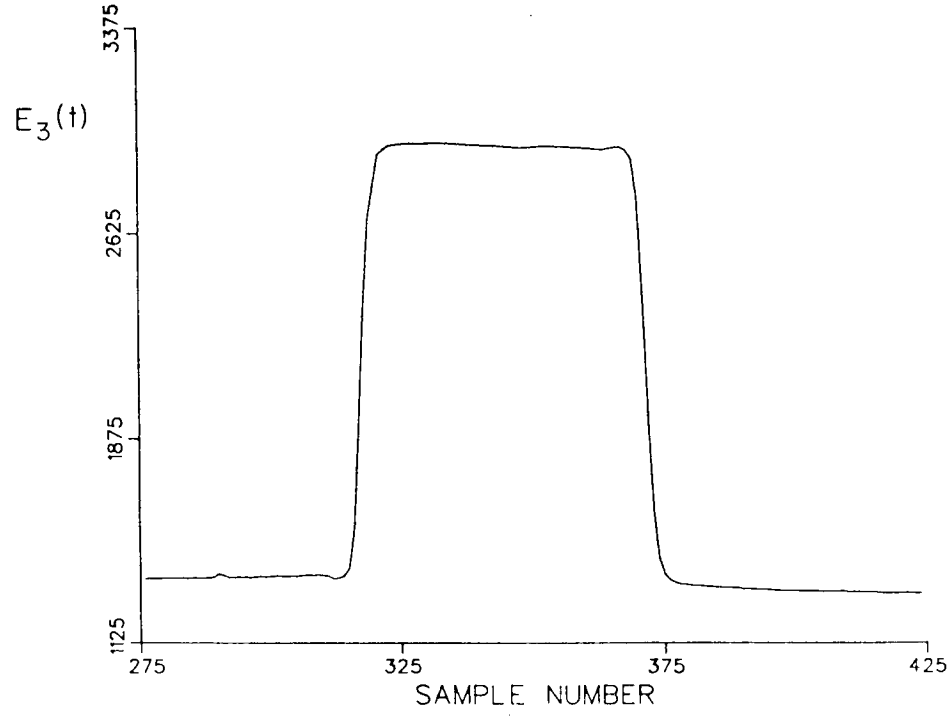

Fig. 7 — Channel 3 of corrected data, extracted from Fig. 5

Table 3 — Performance Summary for Resistive Coupling Artifact Correction (1-bar data). Each channel waveform (e.g. Figs. 3 and 4) manifests two artifacts: a left artifact and a right artifact. The relative amplitude of each artifact, left and right, is tabulated as a "Percent Error," calculated as $(100\ y_n/x_n)$. Columns labeled "Avg" are the numerical average of columns labeled "Left" and "Right." The column labeled "Left" under "Original Data" can be calculated from the values of x_n and y_n in Table 2. The bottom row is an average over channel number, i.e., an array average. Thus, the array-average artifact relative amplitude was 5.6% in the original data, but is reduced tenfold to just 0.55% in the corrected data.

Detector Channel, n	Percent Error $(100\ y_n/x_n)$					
	Original Data			Corrected Data		
	Left	Right	Avg	Left	Right	Avg.
2	4.6	4.3	4.4	0.77	0.35	0.56
3	4.8	4.2	4.5	0.50	0.06	0.28
4	6.1	5.9	6.0	1.01	0.54	0.78
5	5.6	5.6	5.6	0.57	0.67	0.62
6	5.7	5.5	5.6	0.95	0.56	0.76
7	6.8	6.3	6.6	0.70	0.25	0.48
8	6.8	6.4	6.6	1.12	0.40	0.76
9	7.2	6.7	6.9	0.74	0.33	0.53
10	6.7	6.1	6.4	0.38	0.26	0.32
11	6.7	6.2	6.4	0.69	0.23	0.46
12	5.3	5.1	5.2	0.88	0.56	0.72
13	6.6	6.5	6.6	0.68	0.64	0.66
14	5.4	4.7	5.1	0.31	0.05	0.18
15	5.4	5.1	5.2	1.24	0.35	0.80
16	3.5	3.0	3.3	0.60	0.05	0.33
Average	5.8	5.5	5.6	0.74	0.35	0.55

Figure 8 depicts a typical even channel of data obtained against a laboratory target consisting of six vertical bars of varying widths. The data in Fig. 8 were obtained in measurements made about three months subsequent to the Fig. 2 measurements. The correction demonstrated for the six-bar data appears almost as good as for the earlier data. On average, the resistive coupling artifact evidenced by the last bar of the six-bar target is reduced eightfold (Table 4).

We note that the later data were corrected with correction constants derived from the earlier data.

Figures 9a and 9b are provided as a final example of how the resistive coupling artifact appears in original and corrected field data. Figure 9a shows channel 2 of a long-wave scan across the moon, obtained at 8:48 PM on 14 August 1983 during initial sensor field trials at Montauk Point, LI. The local minimum in the neighborhood of sample #330, which is due to the resistive coupling effect, is largely eliminated by application of Eq. (1) to the data (Fig. 9b).

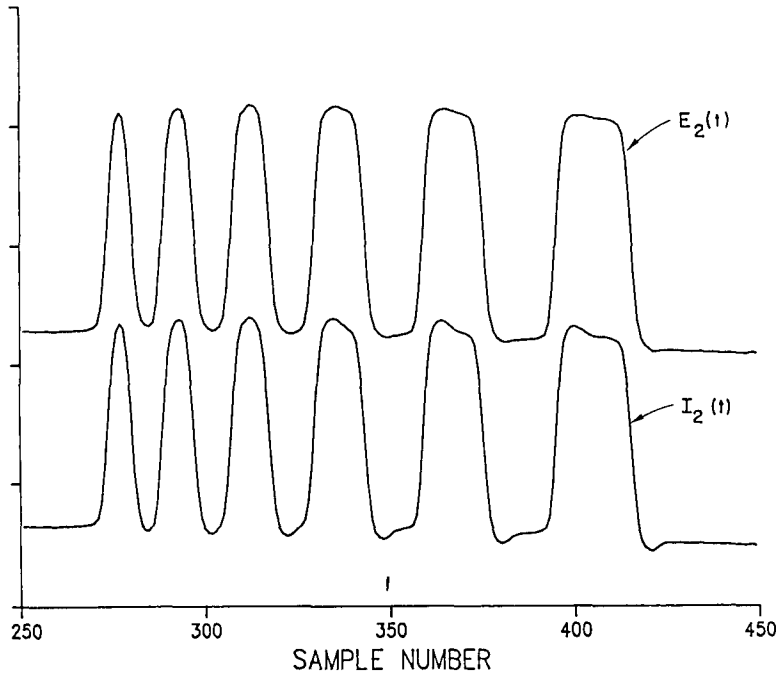

Fig. 8 — Channel 2 of 6-bar data, before (I_2) and after (E_2) resistive coupling correction. Correction constants derived from 1-bar data, Fig. 2, obtained 3 months prior to the 6-bar data.

Table 4 — Performance Summary for Resistive Coupling Artifact Correction (last bar of 6-bar data). Interpretation analogous to Table 3. According to the bottom row in this table, the array-average artifact relative amplitude was 5.6% in the original data, but is reduced eightfold to 0.71% in the corrected data.

Detector Channel, n	Percent Error ($100\ y_n/x_n$)					
	Original Data			Corrected Data		
	Left	Right	Avg	Left	Right	Avg.
2	4.9	3.6	4.3	0.96	0.19	0.58
3	5.3	4.5	4.9	1.13	0.22	0.68
4	6.4	5.1	5.7	1.19	0.53	0.86
5	6.6	5.6	6.1	1.63	0.64	1.14
6	5.9	4.9	5.4	0.95	0.46	0.70
7	6.7	6.3	6.5	0.77	0.31	0.54
8	7.1	5.9	6.5	1.28	0.46	0.87
9	7.3	6.7	7.0	1.06	0.37	0.71
10	6.7	4.8	5.7	0.91	0.20	0.55
11	6.9	5.9	6.4	1.02	0.04	0.53
12	5.5	4.2	4.9	0.97	0.65	0.81
13	7.1	6.2	6.7	1.27	0.36	0.82
14	5.4	4.4	4.9	0.76	0.67	0.71
15	5.8	5.1	5.4	1.05	0.32	0.68
16	3.7	2.2	2.9	0.64	0.41	0.53
Average	6.1	5.0	5.6	1.04	0.39	0.71

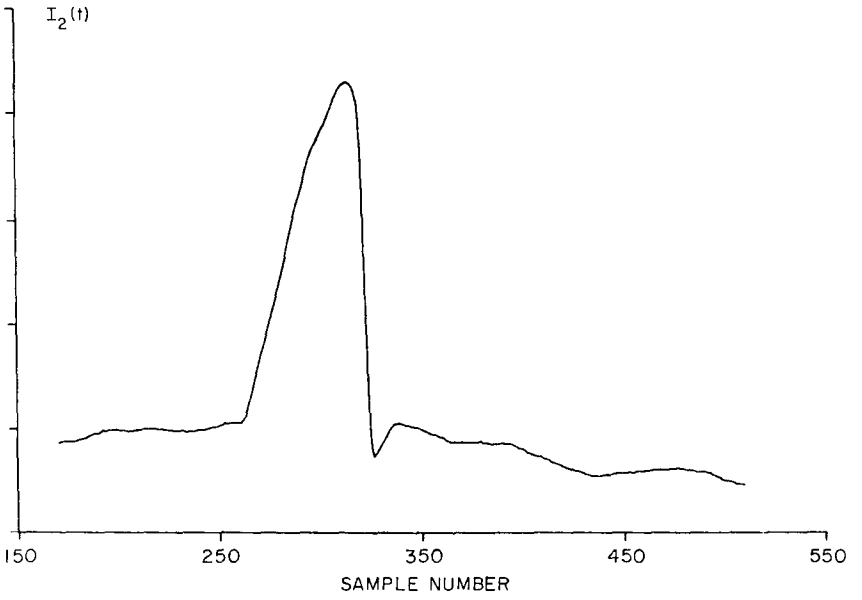

(a)

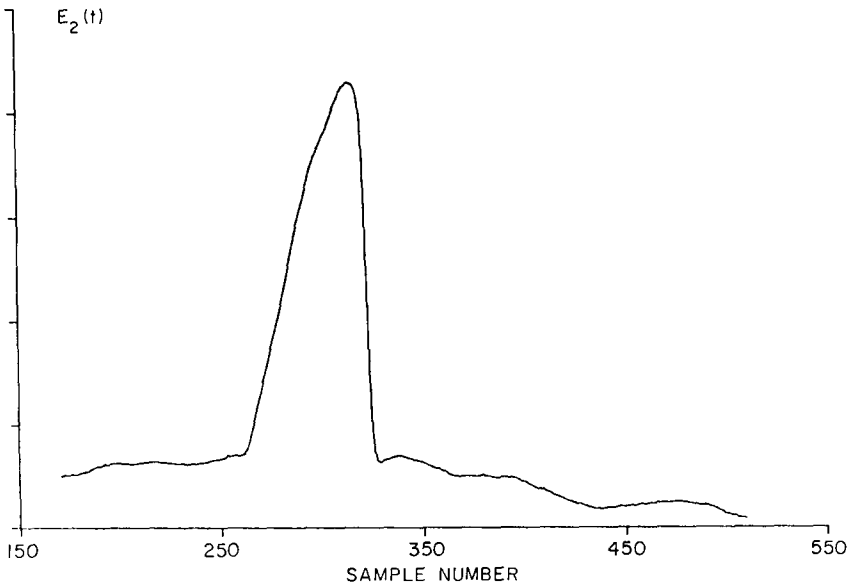

(b)

Fig. 9 — Channel 2 of a long-wave scan across the moon. The artifact appearing near sample #330 in the uncorrected data (part a) is largely eliminated in the corrected data (part b). Data obtained at Montauk Point, LI, at 8:48 PM on 14 August 1983.

FOCAL PLANE EQUIVALENT CIRCUIT

The starting point for our analysis is the preamp/bias circuit diagram and focal plane equivalent circuit, Fig. 10, developed with the aid of Raytheon engineers.

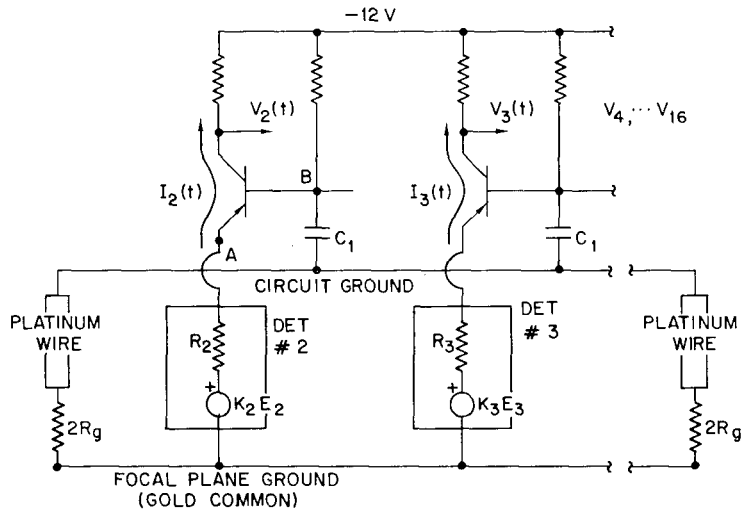

Fig. 10 — Bias/input stage schematic and detector array equivalent circuit for long-wave photoconductive HgCdTe array. Adapted from correspondence between J. Fattel and A. Krutchkoff (Raytheon Missile Systems).

Note that the photoconductor Thévenin equivalent voltages $E_n(t)$ are the "ideal" voltage waveforms that we wish to recover by data reduction (Fig. 10). The measured waveform $V_n(t)$ is proportional to the current $I_n(t)$ flowing through the photoconductor. The circuit ground and focal plane ground (i.e., gold common) have effectively zero resistance. As shown in Fig. 10, the focal plane common and circuit ground are joined by two resistive ground connections that are electrically in parallel. The detector equivalent resistances $R_2, R_3, \ldots R_{16}$, are assumed to be unknown and generally different from one another. Our model is general enough to accommodate nonuniformity in detector responsivity, accounted for as an unknown gain parameter K_n multiplying each of the Thévenin voltage sources in Fig. 10.

Figure 10 can be simplified somewhat by replacing the bias/input stage schematics by equivalent circuits. We note that the voltage drop from transistor emitter to base is a small constant value, i.e., points A and B in Fig. 10 are effectively shorted. Moreover, the large value of capacitor C_1 assures that C_1, also, can be considered effectively a short circuit. The resultant focal plane/input stage equivalent circuit is given in Fig. 11. In this figure we consider the currents $I_n(t)$ as the measurable quantities and voltage sources $E_n(t)$ as the quantities we wish to determine. The 31 constants R_g, R_n, and K_n ($n = 2, 3, \ldots 16$) are all indeterminate at this stage of analysis.

It follows from Fig. 11 that

$$K_nE_n = R_nI_n + R_gI, \quad n = 2, 3, \ldots 16 \tag{2}$$

where

$$I = \sum_{n=2}^{16} I_n. \tag{3}$$

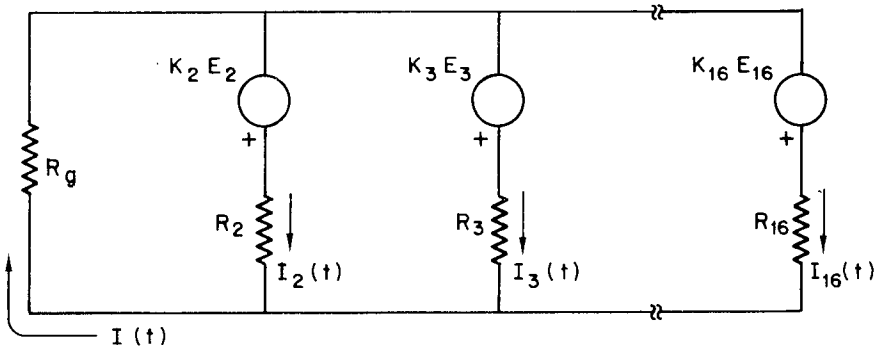

Fig. 11 — Long-wave focal plane/input stage equivalent circuit, corresponding to Fig. 10

The quantities E_n, I_n, and I in Eqs. (2) and (3) are time waveforms, i.e., $E_n(t)$, $I_n(t)$, and $I(t)$. Other quantities, i.e., K_n, R_n, and R_g are time-independent. We see directly from Eq. (2) that if R_g were zero, the desired waveforms $E_n(t)$ would be equal to the measured waveforms $I_n(t)$ to within a readily determined calibration gain. Nonzero R_g, however, causes coupling among the waveforms. Equation (2) may be thought of as an error correction equation: if the constants K_n, R_n, and R_g are known, Eq. (2) can be used to convert the measured uncorrected waveforms I_n into the desired waveforms E_n.

Equation (2) is now written as

$$A_n E_n = I_n + B_n I, \tag{4}$$

where we define

$$A_n \equiv K_n/R_n \,, \tag{5}$$

and

$$B_n \equiv R_g/R_n \,. \tag{6}$$

Summing Eq. (4) for values of n from 2 to 16, using Eq. (3) to simplify the result, and gathering terms in I we obtain

$$I = \left[1 + \sum_{m=2}^{16} B_m\right]^{-1} \sum_{j=2}^{16} A_j E_j \,. \tag{7}$$

Substituting Eq. (7) into Eq. (4) we obtain

$$I_n = A_n E_n - \epsilon_n \sum_{j=2}^{16} A_j E_j \,, \tag{8}$$

where we define

$$\epsilon_n \equiv B_n \left[1 + \sum_{m=2}^{16} B_m\right]^{-1} \,. \tag{9}$$

We think of Eq. (8) as describing how the desired waveforms, $E_n(t)$, are damaged in creating the measured waveforms $I_n(t)$.

From Eqs. (3) and (4),

$$E_n = A_n^{-1}\left\{I_n + B_n \sum_{m=2}^{16} I_m\right\} \,. \tag{10}$$

We can show from Eq. (9) that

$$B_n = \epsilon_n \left[1 - \sum_{m=2}^{16} \epsilon_m \right]^{-1}. \tag{11}$$

Equation (10), like Eq. (2), may be thought of as an error correction equation. Our task is now to obtain values for the 30 constants (A_n, B_n) appearing in Eq. (10).

BAR-TARGET EXCITATION

We now assume that the sensor is scanned across a vertically oriented bar target, so that

$$E_n(t) = \begin{cases} E_e(t), & n = 2, 4, \ldots 16, \\ E_0(t), & n = 3, 5, \ldots 15. \end{cases} \tag{12}$$

The forms of $E_e(t)$ and $E_0(t)$ are schematized in Fig. 12. The odd-numbered waveforms are delayed two dwell-times relative to the even-numbered waveforms due to the gold common being equal in width to the detectors (Fig. 1).

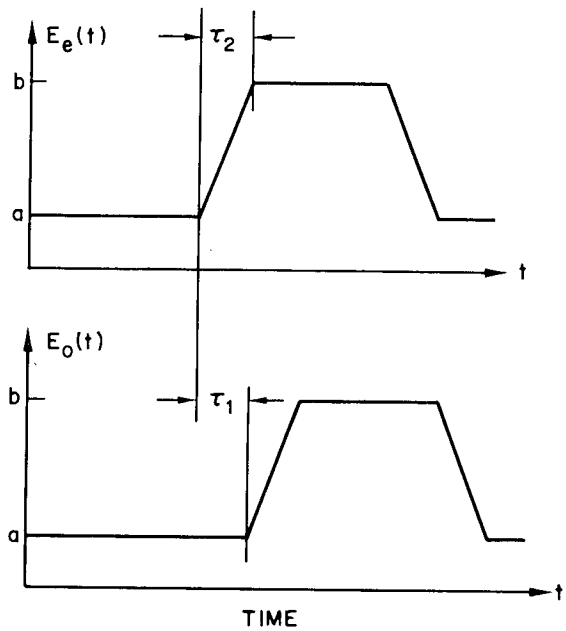

Fig. 12 — Idealized even-channel waveforms, $E_e(t)$, and odd-channel waveforms, $E_0(t)$, for bar target excitation. Waveforms $E_0(t)$ are delayed two dwell-times relative to $E_e(t)$, i.e., $\tau_1 = 2\tau_d$, due to the separation between the even and odd detector columns shown in Fig. 1. Step-response rise-time, τ_2, is assumed also to be two dwell-times, including the effects of optical blur, detector size, and the electrical response characteristics of preamps, and digital recorder.

From Eqs. (8) and (12)

$$I_n = \begin{cases} H_n(E_e - \delta_n E_0), & n \text{ even} \qquad (13a) \\ H_n(E_0 - \delta_n E_e), & n \text{ odd}, \qquad (13b) \end{cases}$$

where we define

$$H_n \equiv \begin{cases} (A_n - \epsilon_n C_e), & n \text{ even} \qquad (14a) \\ (A_n - \epsilon_n C_0), & n \text{ odd}, \qquad (14b) \end{cases}$$

and

$$\delta_n \equiv \begin{cases} \epsilon_n C_0 / H_n, & n \text{ even} \quad (15a) \\ \epsilon_n C_e / H_n, & n \text{ odd.} \quad (15b) \end{cases}$$

Quantities C_e and C_0 in Eqs. (14) and (15) are defined as

$$C_e = \sum_{j=1}^{8} A_{2j}, \quad (16)$$

and

$$C_0 = \sum_{j=1}^{7} A_{2j+1}. \quad (17)$$

For even-numbered channels the form of $I_n(t)$ follows from Eq. (13a), depicted graphically as Figs. 13a and 13b. Also shown as Fig. 13c is a more realistic waveform adapted from Fig. 3. The quantities x_n and y_n shown on Fig. 13c are attributes that may be measured directly from the available waveforms $I_n(t)$.

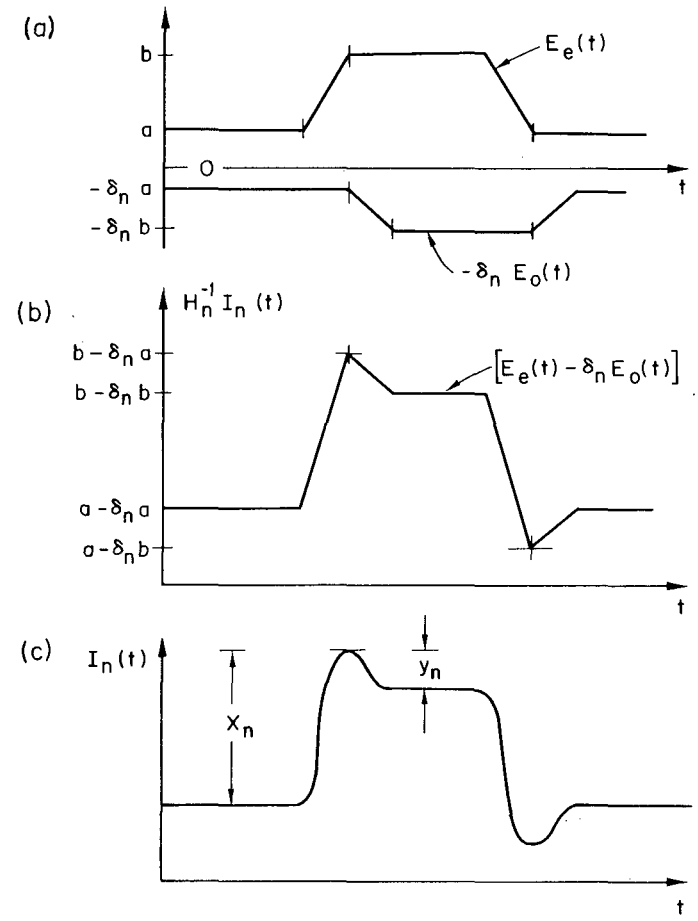

Fig. 13 — (a) and (b) The form of $I_n(t)$ is deduced from Eq. (13a) and Fig. 12, for even-numbered channels. (c) A more realistic waveform adapted from Fig. 3. Equations for the correction constants are obtained by equating corresponding quantities in (b) and (c).

Setting corresponding quantities equal to one another from Figs. (13b) and (13c) we obtain

$$x_n = (b - a)H_n, \tag{18}$$

and

$$y_n = \delta_n(b - a)H_n. \tag{19}$$

Recasting Eq. (18),

$$H_n = x_n/(b - a), \tag{20}$$

and dividing Eq. (19) by Eq. (18),

$$\delta_n = y_n/x_n. \tag{21}$$

Eliminating H_n from Eqs. (14a) and (15a) we obtain

$$A_n = \epsilon_n(C_e + C_0/\delta_n) = \epsilon_n y_n^{-1}(C_e y_n + C_0 x_n), \tag{22}$$

where the final equality is obtained by substituting Eq. (21) for δ_n.

Eliminating H_n from Eqs. (15a) and (20),

$$H_n = x_n/(b - a) = \epsilon_n C_0/\delta_n. \tag{23}$$

Substituting Eq. (21) for δ_n into Eq. (23) we can write

$$\epsilon_n = T_e y_n, \tag{24}$$

where T_e is independent of n. From Eqs. (22) and (24)

$$A_n = T_e(C_e y_n + C_0 x_n). \tag{25}$$

Summing Eq. (25) over even values of n and invoking Eq. (16) we obtain

$$C_e = T_e(C_e Y_e + C_0 X_e), \tag{26}$$

where we define

$$Y_e = \sum_{j=1}^{8} y_{2j}, \tag{27}$$

and

$$X_e = \sum_{j=1}^{8} x_{2j}. \tag{28}$$

Eliminating T_e from Eqs. (24) to (26) we obtain

$$A_n = C_e\left[\frac{C_e y_n + C_0 x_n}{C_e Y_e + C_0 X_e}\right], \quad n \text{ even}, \tag{29}$$

and

$$\epsilon_n = y_n C_e(C_e Y_e + C_0 X_e)^{-1}, \quad n \text{ even}. \tag{30}$$

For odd-numbered channels the form of $I_n(t)$ follows from Eq. (13b), depicted graphically as Figs. 14a and 14b.

We can show analogous to Eqs. (29) and (30) that for odd-numbered channels

$$A_n = C_0\left[\frac{C_0 y_n + C_e x_n}{C_0 Y_0 + C_e X_0}\right], \quad n \text{ odd}, \tag{31}$$

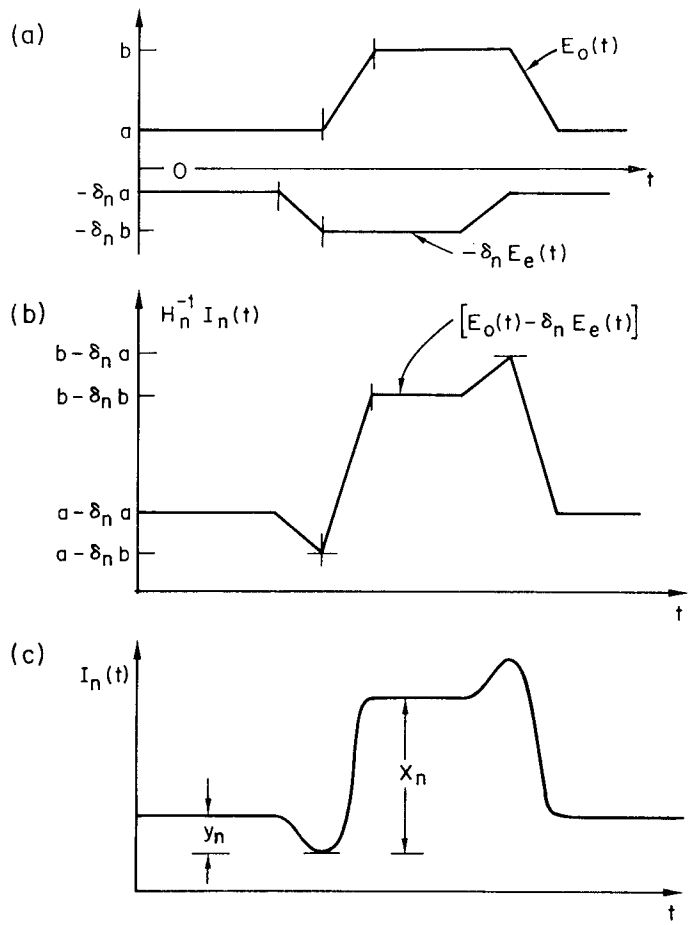

Fig. 14 — (a) and (b) The form of $I_n(t)$ is deduced from Eq. (13b) and Fig. 12, for odd-numbered channels. (c) A more realistic waveform adapted from Fig. 4. Equations for the correction constants are obtained by equating corresponding quantities in (b) and (c).

and

$$\epsilon_n = y_n C_0 (C_0 Y_0 + C_e X_0)^{-1}, \quad n \text{ odd.} \tag{32}$$

In Eqs. (31) and (32) we define the quantities Y_0 and X_0 as

$$Y_0 = \sum_{j=1}^{7} y_{2j+1}, \tag{33}$$

and

$$X_0 = \sum_{j=1}^{7} x_{2j+1}, \tag{34}$$

analogous to Eqs. (27) and (28).

We show in the appendix of this report that, from Eqs. (11), (30), and (32),

$$B_n = R_g/R_n = \begin{cases} y_n \left[\dfrac{Y_0 + (C_e/C_0)X_0}{X_e X_0 - Y_e Y_0} \right], & n \text{ even} \\ y_n \left[\dfrac{Y_e + (C_0/C_e)X_e}{X_e X_0 - Y_e Y_0} \right], & n \text{ odd.} \end{cases} \tag{35}$$

Our correction formula expressed as Eq. (10) has 30 indeterminate constants, 15 values each of A_n and B_n. However we see that if the A_n can be determined, the values of B_n can then be calculated from Eqs. (35), (16), and (17). Thus, our 30 unknowns are presently reduced to 15. (The constants Y_e, X_e, Y_0, and X_0 appearing in Eq. (35) are calculated from Eqs. (27), (28), (33), and (34) in terms of the x_n, y_n values directly measured from the bar target waveforms, e.g., Figs. 3 and 4.)

ITERATIVE SOLUTION

The constants A_n appearing in the data correction equation, Eq. (10), are obtained by iteratively solving Eqs. (29) and (31) according to the following prescription:

$$A_n^{(i+1)} = C_e^{(i)} \left\{ \frac{C_e^{(i)} y_n + C_0^{(i)} x_n}{C_e^{(i)} Y_e + C_0^{(i)} X_e} \right\}, \quad n \text{ even} \tag{36}$$

$$A_n^{(i+1)} = C_0^{(i)} \left\{ \frac{C_0^{(i)} y_n + C_e^{(i)} x_n}{C_0^{(i)} Y_0 + C_e^{(i)} X_0} \right\}, \quad n \text{ odd}, \tag{37}$$

where, from Eqs. (16) and (17),

$$C_e^{(i)} = \sum_{j=1}^{8} A_{2j}^{(i)}, \tag{38}$$

and

$$C_0^{(i)} = \sum_{j=1}^{7} A_{2j+1}^{(i)}. \tag{39}$$

The superscript on quantities A_n, C_e, and C_0 in Eqs. (36) to (39) indicates the order of iteration.

We start the iterative solution by assuming that to zero-order the gains K_n and resistances R_n are the same for all detectors (cf. Fig. 10). From Eq. (5),

$$A_n^{(0)} = 1. \tag{40}$$

Starting with $A_n^{(0)}$ equal to a constant other than unity results in a proportional scaling of the iterative solution for A_n. Since the measurables $V_n(t)$ in Fig. 10 are related to the $I_n(t)$ by an electrical gain, it follows from Eq. (8) that all values of A_n can be scaled by an arbitrary multiplicative constant chosen to suit our convenience.

From Eqs. (38) to (40),

$$C_e^{(0)} = 8 \tag{41}$$

$$C_0^{(0)} = 7. \tag{42}$$

The next order of approximation beyond Eq. (40) follows from Eqs. (36), (37), (41), and (42),

$$A_n^{(1)} = \begin{cases} 8 \left\{ \dfrac{8 y_n + 7 x_n}{8 Y_e + 7 X_e} \right\}, & n \text{ even} \\ 7 \left\{ \dfrac{7 y_n + 8 x_n}{7 Y_0 + 8 X_0} \right\}, & n \text{ odd}. \end{cases} \tag{43}$$

The parameters x_n and y_n in Eq. (43) are directly measurable from the bar target data, e.g., Figs. 3 and 4.

The numerical values $A_n^{(1)}$ obtained from Eq. (43) are substituted into Eqs. (38) and (39) to obtain $C_e^{(1)}$ and $C_0^{(1)}$, which in turn are substituted into Eqs. (36) and (37) to obtain $A_n^{(2)}$. Convergence is achieved to eight places after four iterations.

The fully converged solution for A_n is used with Eqs. (16), (17), and (35) to obtain the remaining correction constants, B_n.

The waveform parameters x_n, y_n obtained from the Fig. 2 waveforms and the corresponding iterative solutions for A_n^{-1} and B_n are given in Table 2.

CONCLUSIONS

As shown in the numerical examples discussed in our Summary of Results, illustrated in Figs. 2 to 9, excellent correction has been achieved for data defects caused by resistive interchannel coupling. The correction constants derived from a "diagnostic frame," Fig. 2, provide accurate correction to scenes containing different varieties of structure and obtained months after the diagnostic frame. Thus, the correction constants are time- and data-independent. Nonetheless, we intend to obtain diagnostic frames both immediately before and immediately after each field trial with the Raytheon sensor to assure a completely updated set of long-wave resistive coupling correction constants for use in data reduction.

The instantaneous, "memoryless," nature of the resistive coupling defect allows us to perform correction without smoothing the data, i.e., without loss of spatial resolution. The form of the correction equation, Eq. (10), together with the fact that $B_n = O(10^{-2})$, implies that the relative increase in rms sensor noise introduced by the correction process is a small fraction of 1%, and hence is negligible.

ACKNOWLEDGMENTS

The resistive coupling mechanism responsible for the spatial defect was originally identified by Andre Krutchkoff and Jean Fattel (Raytheon Missile Systems Division, Bedford, MA). Mr. Fattel also contributed the preamp/bias input stage schematic, Fig. 10. Infrared scanner measurements were performed and made available by Joseph DiBiaso, Andre Krutchkoff, and Irving Goldstein (Raytheon/Bedford). Extraction of waveform parameters x_n and y_n from the diagnostic bar target data is performed with software developed by Brent Lander (JAYCOR, Alexandria, VA). Data correction and display are performed with software developed by Brian Sweeney (Sachs/Freeman Assoc., Bowie, MD).

The assistance of George Roberts and Gene Robillard (New England Research Center, Sudbury, MA) in providing detailed technical information on the HgCdTe detector array is gratefully acknowledged.

The Raytheon dual-band scanner is a uniquely valuable tool for the development of advanced IR search and track devices. The small, correctable, artifact discussed in this report in no way subtracts from the remarkable technical accomplishments of Raytheon and New England Research Center in the fabrication of the scanner and its long-wave array.

REFERENCES

1. R. Steinberg, "Navy IR Backgrounds Measurement and Analysis Program," Proceedings of the Tri-Service Infrared Backgrounds Symposium, 18-20 Oct. 1983, Air Force Geophysics Laboratory.

2. R. Steinberg, "Infrared Background Sensor Characterization and Data Reduction," Proceedings of the Infrared Information Symposium, Specialty Group or Targets, Backgrounds, and Discrimination, 1-2 February 1984.

Appendix

DERIVATION OF EQUATION (35)

From Eqs. (30) and (27)

$$\sum_{n=1}^{8} \epsilon_{2n} = C_e Y_e (C_e Y_e + C_0 X_e)^{-1}. \tag{A1}$$

From Eqs. (32) and (33)

$$\sum_{n=1}^{7} \epsilon_{2n+1} = C_0 Y_0 (C_0 Y_0 + C_e X_0)^{-1}. \tag{A2}$$

Adding Eqs. (A1) and (A2), and subtracting the resultant from unity, we can show that

$$\left\{1 - \sum_{m=2}^{16} \epsilon_m\right\} = \frac{C_e C_0 (X_e X_0 - Y_e Y_0)}{(C_0 Y_0 + C_e X_0)\ (C_e Y_e + C_0 X_e)}. \tag{A3}$$

From Eqs. (A3), (30), and (32),

$$B_n = \epsilon_n \left\{1 - \sum_{m=2}^{16} \epsilon_m\right\}^{-1} = \begin{cases} y_n \left\{\dfrac{Y_0 + (C_e/C_0) X_0}{X_e X_0 - Y_e Y_0}\right\}, & n \text{ even} \\ y_n \left\{\dfrac{Y_e + (C_0/C_e) X_e}{X_e X_0 - Y_e Y_0}\right\}, & n \text{ odd.} \end{cases} \tag{A4}$$

Equation (A4) is given as Eq. (35) in the main text.